Jansson and Brydegaard *Anim Biotelemetry (2018) 6:6*
https://doi.org/10.1186/s40317-018-0151-5

Animal Biotelemetry

RESEARCH

Open Access

Passive kHz lidar for the quantification of insect activity and dispersal

Samuel Jansson[1,2*] and Mikkel Brydegaard[1,2]

Abstract

Background: In recent years, our group has developed electro-optical remote sensing methods for the monitoring and classification of aerofauna. These methods include active lidar methods and passive, so-called dark-field methods that measure scattered sunlight. In comparison with satellite- and airborne remote sensing, our methods offer a spatiotemporal resolution several orders of magnitude higher, and unlike radar, they can be employed close to ground. Whereas passive methods are desirable due to lower power consumption and ease of use, they have until now lacked ranging capabilities.

Results: In this work, we demonstrate how passive ranging of sparse insects transiting the probe volume can be achieved with quadrant sensors. Insects are simulated in a raytracing model of the probe volume, and a ranging equation is devised based on the simulations. The ranging equation is implemented and validated with field data, and system parameters that vary with range are investigated. A model for estimating insect flight headings with modulation spectroscopy is implemented and tested with inconclusive results. Insect fluxes are retrieved through time-lag correlation of quadrant detector segments, showing that insects flew more with than against the wind during the study period.

Conclusions: The presented method demonstrates how ranging can be achieved with quadrant sensors, and how it can be implemented with or without active illumination. A number of insect flight parameters can be extracted from the data produced by the sensor and correlated with complementary information about weather and topography. The approach has the potential to become a widespread and simple tool for monitoring abundances and fluxes of pests and disease vectors in the atmosphere.

Keywords: Near-field optics, Lidar, Remote sensing, Aerofauna, Dark field, Modulation spectroscopy

Background

Insects are a diverse group of animals with a large impact on human society. They cause a large amount of human deaths annually [1] and effect significant economic damage in forestry [2] and agriculture [3]. Pesticides employed to combat this can have severe health effects for humans [4] and pollinators [5]. Insect activity and movement patterns occur on fast timescales [6], are complex and species specific [7], and can be highly localized [8]. As such, a high spatiotemporal resolution is required to monitor their movements, activity patterns, and interactions.

A number of methods have been developed to investigate the phenology of insects in situ. Vehicle-mounted sweep nets [9], human landing catch, electrocuting grids [10], and insect traps [11] are commonly employed for directly monitoring insect behavior and abundances. These methods can provide rich information on insects, but are laborious and yield relatively low counts. Air- and satellite-borne topographical remote sensing methods, including imaging and light detection and ranging (lidar), are commonplace. In these, indirect observations of insect activity are made through correlation with the profiled vegetation structure [12, 13]. By relying on the passage of aircraft or satellites, these indirect methods

*Correspondence: samuel.jansson@forbrf.lth.se
[1] Lund Laser Centre, Department of Physics, Lund University, Sölvegatan 14, 22362 Lund, Sweden
Full list of author information is available at the end of the article

are restricted to a time resolution in the order of days or weeks, and satellite imaging typically has a spatial resolution of 30×30 m^2. Radar entomology is a method wherein direct observations of insects are made through the transmission and measurement of backscattered microwave pulses [14–16]. Radar systems have a demonstrated species classification capability [17], but are unable to monitor horizontally close to ground due to clutter effects.

Lidar entomology is an emerging field in which laser transects across the landscape are monitored [18–20]. We have experience recording over a hundred thousand insect observations per hour [21], and species classification through modulation spectroscopy of insect wing beats has been demonstrated [11, 22–24]. Entomological lidar systems typically have a spatial resolution in the order of centimeters and a temporal resolution in the order of microseconds. Our group has also developed passive, so-called dark-field methods [25] based on sunlight illumination of the field of view (FOV). Remote dark-field methods yield comparable results to entomological lidar, but with much simpler instrumentation [26, 27]. By relying on sunlight, these methods are limited to daytime use and clear-sky conditions. Until now, passive dark-field methods have not been thought to provide range information.

Without range information, it is challenging to quantify the scattering cross section of a target. A number of methods have been developed to tackle this problem. Techniques such as nephelometry and flow cytometry [28] limit the probe volume to a point, allowing precise measures of the scattering properties of passing sparse particles in a limited volume. Other methods instead assess particle sizes in extinction mode. In digital in-line holography [29], the sparse intersection of zooplankton with the probe volume generates a diffraction pattern on a sensor. Through post-focusing, measures of size and position are obtained. These techniques utilize active laser illumination of the FOV in order to enable ranging. Compared to laser-based techniques, passive techniques benefit from reduced complexity, cost, weight, and power consumption. Laser eye safety considerations and radiation legislation are avoided, but operation is limited to daytime use and often clear-sky conditions. The strongest signal from aerofauna is obtained in backscatter mode, which puts constraints on the FOV orientation.

This work investigates whether optical ranging of sparsely distributed insects intersecting the probe volume of a quadrant sensor in the near-field can be achieved. A ranging equation based on a raytracing model is introduced and tested on field data. The estimated range to observed insects is used to evaluate the scattering processes in and along the probe volume. In addition to evaluating the ranging capabilities of quadrant sensors, we investigate the validity of a previously proposed model suggesting a relationship between the flight heading of insects and the frequency contents of the received signal [30]. Finally, we test the method's capability of profiling vertical and horizontal insect fluxes.

Methods

Numerical and analytical considerations

The detection scheme consists of a quadrant photodiode (QPD) in the image plane of a Newtonian telescope. The QPD is focused at a known distance, r_{foc}, which coincides with the position of a black termination cavity. As such, the QPD is unfocussed at the aperture but is gradually focused along the FOV toward r_{foc}. Expressed differently, the FOV of the QPD segments overlap entirely at the telescope aperture, and are gradually separated with distance until imaged sharply at r_{foc}. In this setup, the FOV is assumed to be evenly illuminated by the sunlight and is therefore equivalent to the probe volume. The properties of the imaging system are illustrated in Fig. 1.

We further make the following assumptions:

1. The observed insects are small compared to the probe volume (corresponding to point sources when illuminated by homogeneous sunlight).
2. Throughout the duration of an observation, the insect velocity vector is constant.
3. The coaxial movement of the observed insects is limited compared to the length of the probe volume.

When an insect transits the probe volume, sunlight is scattered into the telescope and an intensity increase is recorded. The signal includes a low-frequency envelope from the insect body and an oscillatory component from the insect wings [30, 31]. As observed in Fig. 1d), the signal recorded in two adjacent detector elements is identical at close range, differs but blends together at medium range, and is sharply resolved at far range. The overlap can be quantified through time-lag correlation of the detector segments, which is the cross-correlation between the two time vectors obtained by the detector elements as a function of sliding delay. The delay time, τ, then corresponds to the maximum correlation. τ increases linearly with range, as seen in Fig. 1d), and is inversely proportional to the flight speed of insects. The flight speed is eliminated by dividing τ with the transit time Δt, yielding a quotient that is unique for each range. The distance $\hat{r}$ to an insect transiting the probe volume is estimated according to Eq. 1.

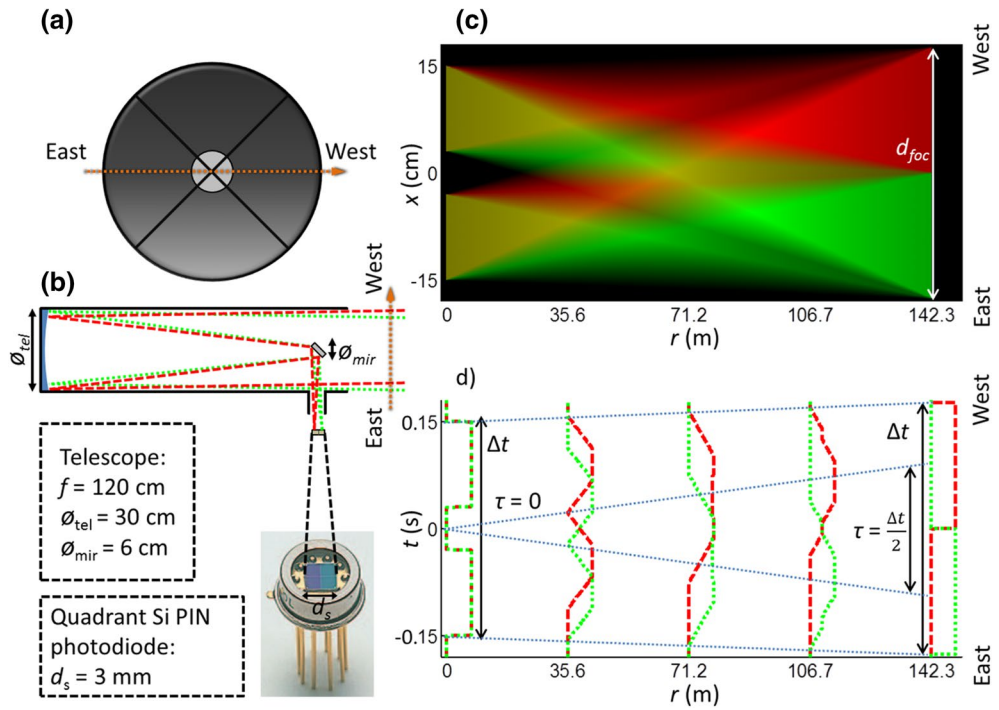

Fig. 1 **a** Newtonian aperture as seen from the front, with a simulated insect trajectory marked in orange. **b** Illustration of the telescope imaging from above, showing that two adjacent QPD elements receive light from slightly different directions. **c** Raytracing of the FOV of two adjacent detector elements, where the eastern FOV is marked in green and the western FOV is marked in red. Positions where the fields overlap are marked in yellow. **d** Simulated signals from point scatterers transiting the probe volume from east to west with a speed of 1 m/s at different distances. The ranging parameters τ and Δt are shown in blue

$$\hat{r} = \frac{\tau \varnothing_{\text{tel}} f}{\tau\left(\frac{\varnothing_{\text{tel}} f}{r_{\text{foc}}} - d_{\text{s}}\right) + \Delta t \frac{d_{\text{s}}}{2}}. \tag{1}$$

In Eq. 1, $\varnothing_{\text{tel}}$ is the telescope aperture, f is the telescope focal length and d_{s} is the quadrant sensor width. The validity of Eq. 1 can be evaluated with the simulated insect signals in the raytracing model, where the distance is known. Equation 1.1 is obtained by rearranging Eq. 1. d_{foc} is the width of the sensor image in the focal plane as calculated with the lens equation (see Fig. 1c). $\alpha = \varnothing_{\text{tel}}/d_{\text{foc}}$ is the quotient of the width of the FOV at the telescope location and the width of the FOV at termination, i.e., the inverse of the linear scaling coefficient of the FOV.

$$\frac{\hat{r}}{r_{\text{foc}}} = \frac{\alpha \frac{2\tau}{\Delta t}}{(\alpha - 1)\frac{2\tau}{\Delta t} + 1} \tag{1.1}$$

The FOV converges if it is terminated in the near-field and diverges if it is terminated in the far-field. If the FOV is terminated at the limit between the near- and far-field, r_{lim}, it maintains a constant width along the monitored transect. In other words, if $r_{\text{foc}} = r_{\text{lim}}$, the quotient α is equal to 1. The distance to termination therefore has implications on the ranging properties; see Fig. 2. The setup parameters given in Fig. 1 yield a limit between near- and far-field $r_{\text{lim}} = 121.2$ m.

Aside from r_{foc}, there are other setup and observation parameters that affect the ranging accuracy. Equation 1 includes the quotient $\tau/\Delta t$ and is therefore invariant to the flight speed of insects. τ is equal to 0 at the aperture and $\Delta t/2$ at termination (see Fig. 1d). Δt depends on the cruise altitude of insects at close range due to the round aperture of the telescope, but is invariant to cruise altitude at far range due to the quadratic shape of the sensor. The quotient $\tau/\Delta t$ is equal to 0 at the aperture and increases linearly with range to 1/2 at termination, indicating that the ranging equation as a whole is invariant to cruise altitude. The climb and heading angles with which insects transit the probe volume can affect the results of Eq. 1. However, this effect is minute since the insect transit distance along the optical axis is negligible in comparison to the length of the probe volume (assumption 3).

Field measurements and insect observation properties

Experiments were carried out on 2013-07-20 between 12:00 and 15:20 at Stensoffa in Southern Sweden

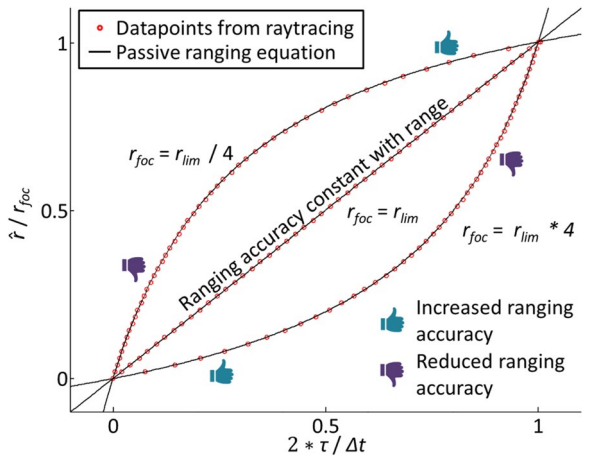

Fig. 2 Illustration of how the ranging properties scale with the length of the FOV. When the distance to the focal plane of the sensor, r_{foc}, is equal to the limit between near- and far-field, r_{lim}, the width of the FOV is constant and the ranging accuracy is unaffected by the distance between the telescope and insect. If the focal plane is located in the near-field, the FOV converges and the method becomes less accurate at close range and more accurate at far range, whereas if the focal plane is located in the far-field, the opposite holds true

(N55.70, E13.45). A quadrant photodiode (Hamamatsu S4349 Si PIN) was used to monitor an air volume through a Newtonian telescope with a focal length of 120 cm and a diameter of 30 cm. The detector has a bandwidth of 2.9 kHz and was sampled at 20 kHz with a data acquisition board (NI USB-6211). The telescope was aimed roughly north in order to collect insect data in backscatter mode. A black termination cavity was placed at a distance of 142.3 m from the telescope, where the detector was focused. The setup, measurement principle, and site are shown in Fig. 3. More details on the experiments are found in [32].

The sunlight propagates through the atmosphere before impinging on the FOV of the detector. As such, turbulence and other atmospheric phenomena can cause rapid variations in the optical background. By filtering the signal with a sliding median, the optical background was obtained. The noise level was obtained as the difference between the optical background and a sliding minimum filtered signal. A detection threshold with signal-to-noise ratio SNR = 2 was set.

A set of harmonic basis functions $\psi_n(t)$ was constructed based on test frequencies $f_{0\text{test}}$. This is described by Eq. 2. The backscattered signal intensity from an insect contains light scattered in the insect body and in the insect wings, $I_{\text{tot}}(t) = I_{\text{body}}(t) + I_{\text{wing}}(t)$. These two signal components were separated using a sliding minimum filter with a window width equivalent to the period of $f_{0\text{test}}$. The estimated wing-beat signal $\hat{I}_{\text{wing}}(t)$ was expressed as a linear combination of basis functions with coefficients a_n as expressed in Eq. 3. $\hat{I}_{\text{wing}}(t)$ was fitted against the original wing-beat data $I_{\text{wing}}(t)$. By scanning $f_{0\text{test}}$ and minimizing the residuals of the fit, a final value for the wing-beat frequency f_0 was obtained. This process is further detailed in [31].

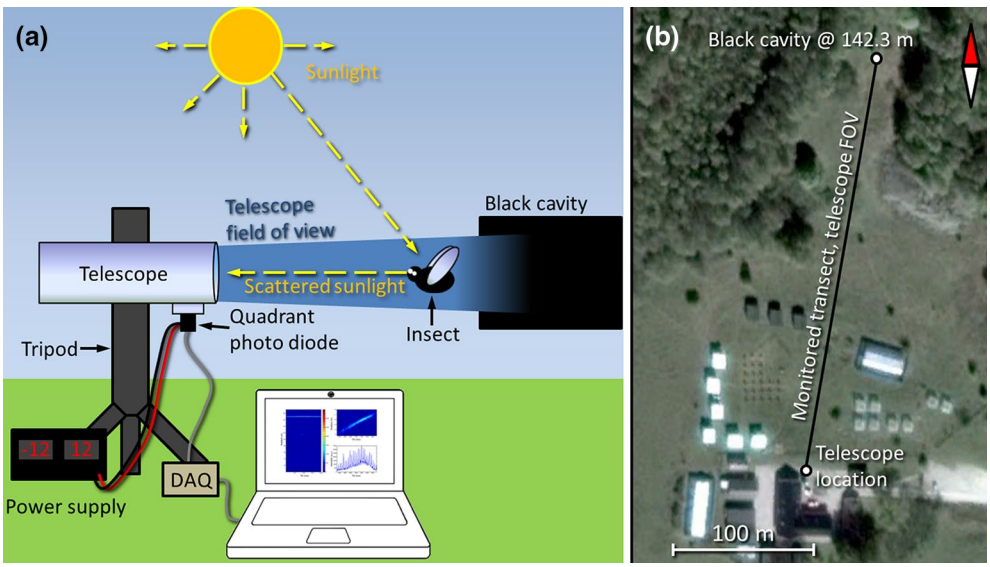

Fig. 3 **a** Illustration of the setup and measurements. A QPD is monitoring an air volume through a telescope. The FOV is terminated in a black cavity to reduce the optical background. When an insect transits the FOV, sunlight is scattered into the telescope and recorded by the sensor. The QPD is sampled continuously with a DAQ board, and the signal is stored in a computer. **b** Map of the measurement site at Stensoffa in Southern Sweden (N55.70, E13.45). The telescope is aimed into a black cavity located 142.3 m away in a roughly northwards direction

$$\psi_n(t) = \sin\left(2\pi n f_{0\text{init}} t\right) + \cos\left(2\pi n f_{0\text{init}} t\right), \quad n = 0, 1, 2, \ldots \tag{2}$$

$$\hat{I}_{\text{wing}}(t) = \sum_n a_n \psi_n, \quad a_n(t) = \left(\psi_n^T \psi_n\right)^{-1} \psi_n^T I_{\text{wing}} \tag{3}$$

I_{tot} vectors can be obtained separately in the signals from the four detector elements. The east–west and up–down time delays, τ_{ew} and τ_{ud}, were obtained through time-lag correlation of the corresponding I_{tot} vectors. $\hat{r}$ was calculated according to Eq. 1 with τ obtained as a weighted average of τ_{ew} and τ_{ud}, see Eq. 4.

$$\tau = \frac{\tau_{\text{ew}} \cdot I_{\text{body\_e}} \cdot I_{\text{body\_w}} + \tau_{\text{ud}} \cdot I_{\text{body\_u}} \cdot I_{\text{body\_d}}}{I_{\text{body\_e}} \cdot I_{\text{body\_w}} + I_{\text{body\_u}} \cdot I_{\text{body\_d}}}, \tag{4}$$

Results

All observations exceeding the detection threshold in two or more bands were considered, yielding a total of 1279 insect observations. Six hundred and fifty were discarded due to a lack of wing-beat information or strong background fluctuations. The remainder were parameterized according to Eqs. 3 and 4, and a further 131 observations were discarded based on the residuals of the fit. The raw signal $I_{\text{body}}(t)$ and $I_{\text{wing}}(t)$ are shown together with the reconstructed waveform from the parameterization $\hat{I}_{\text{wing}}(t)$ in Fig. 4.

For the remaining 498 observations, the east–west and the up–down time delay, τ_{ew} and τ_{ud}, was obtained through time-lag correlation of I_{tot} between the respective detector segments. $\hat{r}$ was calculated according to Eq. 1 using the weighted average of τ_{ew} and τ_{ud} from Eq. 4. Figure 5 shows how τ_{ew} is obtained by keeping the waveform from one detector segment fixed and scanning the other. That way the time delay yielding the maximum correlation can be determined.

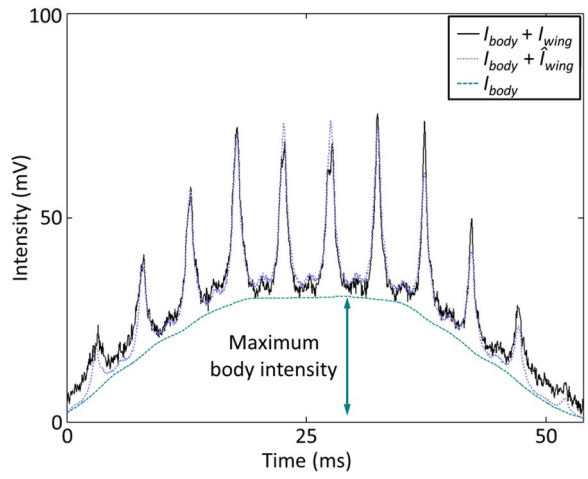

Fig. 4 Raw- and parameterized insect wing signals I_{wing} and $\hat{I}_{\text{wing}}$, shown together with the body signal I_{body} obtained with a sliding minimum. The parameterized signal $\hat{I}_{\text{wing}}$ is constructed from a discrete series of harmonics, the relative strengths and phases of which are obtained by fitting the series onto the raw data and minimizing the residuals of the fit

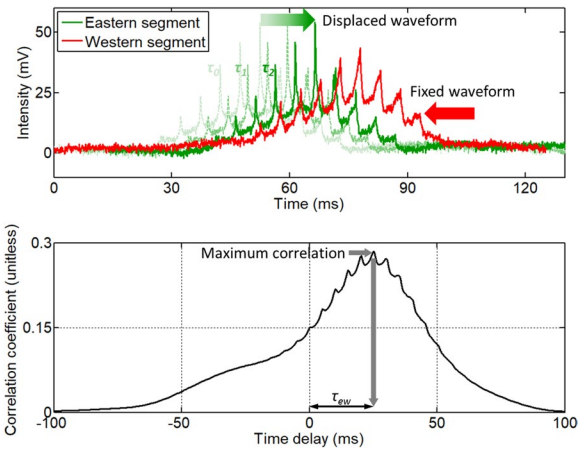

Fig. 5 Top: the retrieved waveforms from an insect in the eastern- and western segments of the detector. As one waveform is kept fixed, the other is gradually displaced with increasing time delay. At each point, the correlation between the two waveforms is calculated. Bottom: the correlation as a function of displacement, or time delay, between the two waveforms. The time delay τ, which is the weighted average of τ_{ew} and τ_{ud}, corresponding to the maximum correlation is used to determine the distance to the insect according to Eq. 1

Figure 6 shows the waveforms and power spectra of three observations at different estimated distances $\hat{r}$. The signal shapes closely resemble our understanding from Fig. 1d). An observation at close range has a large overlap between segments and a signal decrease mid transit due to passing in front of the secondary mirror of the telescope. An observation at medium range has smooth flanks and reduced overlap, whereas an observation at far range has sharp flanks and little overlap between detector segments.

As in conventional lidar, radar, and sonar, the signal attenuates with range. This implies that the system sensitivity is range dependent. The maximum body intensity of insect observations with range can be utilized to investigate the range dependence of the sensitivity. According to the inverse-square law for electromagnetic radiation, the scattered light intensity from insects transiting the FOV is expected to decrease with the square of the distance to the detector. Figure 7 shows a scatterplot of all observations together with isoparametric curves of the inverse-square law, with predicted range $\hat{r}$ and the maximum body intensity of the observations on the axes.

The maximum body intensity is connected to the heading of insects. When an insect impinges on the FOV at a

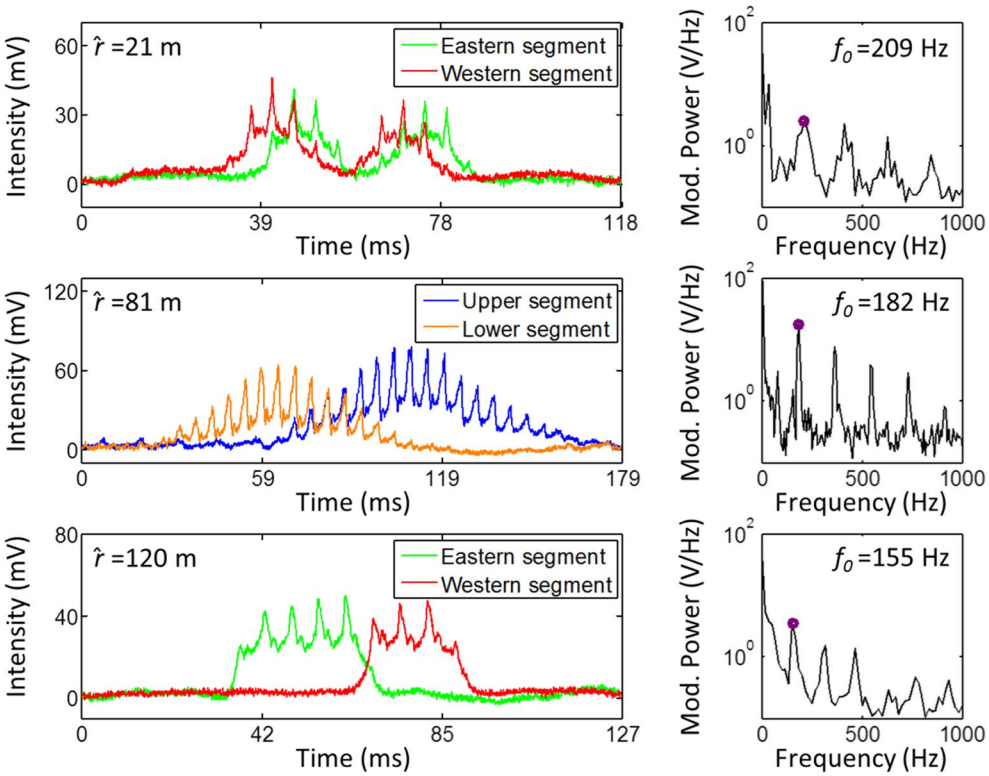

Fig. 6 Examples of insect observation time series and power spectra, from which the ranging parameters τ and Δt, the wing-beat frequency f_0, as well as other observation parameters are extracted. Top: insect signal with a waveform matching close-range simulation (see Fig. 1d). The insect appears in all four detector segments, as expected due to their FOV overlapping at close range, and insertion into Eq. 1 yields a predicted range $\hat{r}$ of 21 m. Middle: signal from an insect entering the FOV with an inclination, appearing in the upper, lower and western detector segments. The waveform matches mid-range simulation, and insertion into Eq. 1 yields a predicted range $\hat{r}$ of 81 m. Bottom: insect signal with a waveform matching far-range simulation, appearing in the eastern, western, and upper detector segments. Insertion into Eq. 1 yields a predicted range $\hat{r}$ of 120 m. The wing-beat frequency f_0 is marked in the power spectrum in all three cases, and can be used for target classification

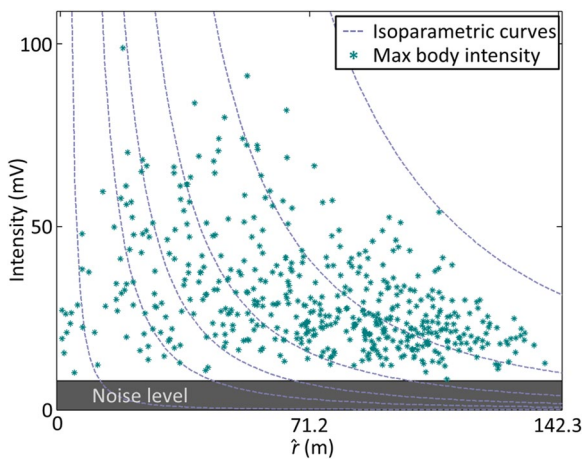

Fig. 7 Scatterplot of observations against predicted range and maximum body intensity, shown together with isoparametric curves of the inverse-square law. The noise level is marked in the figure. A trend of decreasing maximum body intensities with range can be noted among the insect observations

low incident angle, it is observed from the side, appears large, and transits the probe volume quickly. When entering at a high incident angle, it is observed from the front or back, appears small, and stays in the probe volume for an extended period of time. In order to properly evaluate the system sensitivity and quantify the insect scatter signal, the heading angle of insects has to be taken into account. It has been stipulated that the relative strengths of the lower harmonics are tied to the insect heading in relation to the FOV, and a model was presented in [28]. The model suggests that as insects are observed from the front, their wings appear large once per wing-beat cycle which yields a strong fundamental frequency. When instead observed from the side, the wings appear large twice per cycle which results in a strong first overtone. In this study, no relation between the relative strengths and phases of the lower harmonics and the heading angle could be ascertained. Instead, plenty of examples could be found where insect observations with a long transit time had a strong first overtone, and where insect

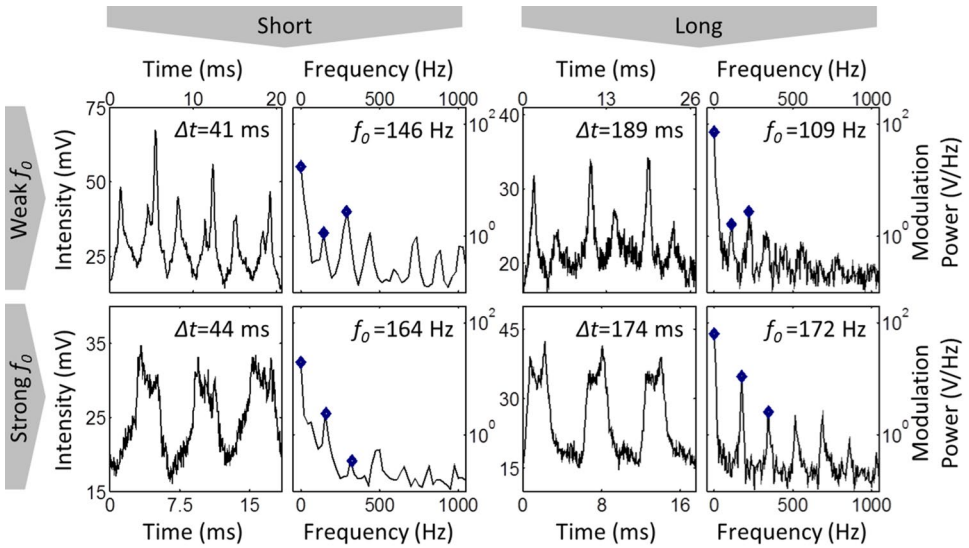

Fig. 8 Fractions of four sample observations. Two are in agreement with the proposed heading model, and two are in disagreement. For each observation, three wing-beat periods are shown together with the frequency contents of the signal up to 1 kHz. Top left: short insect observation with a strong first overtone, similar to what would be expected from an insect entering the FOV at a normal angle. Top right: long insect observation with a strong first overtone, in disagreement with the proposed heading model. Bottom left: short insect observation with a strong fundamental frequency, in disagreement with the proposed model. Bottom right: long insect observation with a strong fundamental frequency, similar to what would be expected from an insect entering the FOV at a large angle and flying along it

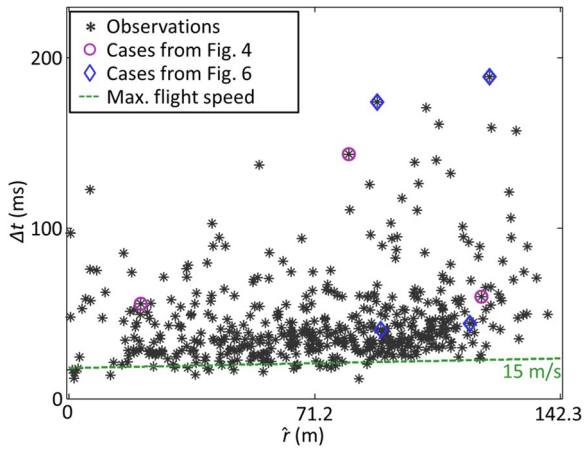

Fig. 9 Scatterplot of insect observations, with predicted range $\hat{r}$ and transit time Δt on the axes. As seen in the figure the transit time increases with predicted range, as expected due to the diverging FOV

observations with a short transit time had a strong fundamental frequency; see Fig. 8.

Insect transit times are range dependent due to the diverging FOV. The FOV cross-section warps from a circle with a 30-cm diameter at the aperture to a square with a 35-cm side at termination. This implies that the insect transit time is affected by cruise altitude at close range but not at far. The effective FOV diameter at each range can be calculated from a linear combination of the geometrical center-of-mass of a circle and a square. Figure 9 shows a scatterplot of insect observations against predicted range $\hat{r}$ and transit time Δt. A flight speed isocurve is also plotted based on the calculated effective FOV diameter.

As seen in Fig. 9, no insect observations at far ranges go below the 15 m/s line, whereas at closer ranges they do. This is an effect of the warping nature of the probe volume. The flight speed is calculated from the effective FOV diameter, which is a center-of-mass approximation. At short range, some insects transit the FOV with a shorter trajectory than the effective diameter, thereby ending up below the line. These insects do not necessarily fly faster than the ones at far range, but remain in the probe volume for a shorter time due to the shorter trajectory. It is also noted that insects with a high incident angle remain longer in the FOV. Therefore, their flight speed cannot be accurately gauged without knowledge of their heading. Presumably, a majority of the observations did not have a flight heading perpendicular to the FOV, and therefore only the shortest transit times are indicative of actual flight speed.

Aside from the presented ranging method, other useful information regarding insect flight in relation to weather and topography can be extracted from quadrant detectors. Figure 10 shows the statistical distribution of τ_{ew}

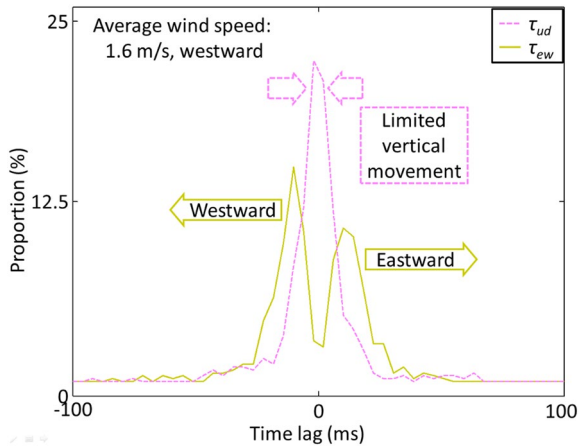

Fig. 10 Histograms of the east–west and up–down time delays, τ_{ew} and τ_{ud}. The east–west distribution is bimodal, indicating that the observed insects transit the probe volume laterally, whereas the up–down distribution is single-modal and centered around 0 ms, indicating that vertical movement is limited. Throughout the study period, the wind was mostly blowing westward, with an average wind speed of 1.6 m/s

and τ_{ud}, and the average wind speed and direction during the study period is presented.

Discussion

In this work, we demonstrated a novel method for extracting range information from insect observations in passive dark-field quadrant measurements. The derived ranging equation was applied to field observations of insects and validated. The range-dependent system sensitivity was investigated. A previously suggested model using modulation spectroscopy was proven insufficient for determining insect flight headings. Insect transit times at different ranges were compared to discreet flight speeds. The insect flight headings were also investigated using time-lag correlation, demonstrating the method's capability of profiling vertical and horizontal insect fluxes. It was shown that most insects transiting the probe volume during the study period were flying laterally with the wind.

The obtained ranging Eqs. 1 and 1.1 depend on the dimensionless quotient $\tau/\Delta t$ and are therefore independent of the shape of the probe volume. This quotient is equal to 0 at the aperture due to the FOV overlap, and scales linearly with range to 1/2 at the termination. As such, both circular and quadratic sensors and apertures can be utilized without affecting the ranging properties.

In order to properly evaluate the system sensitivity with range, the insect flight headings have to be known. Due to their elongated shape, insects display different optical cross sections when observed and illuminated from different angles. Target classification can be accomplished through modulation spectroscopy, and would also aid in the evaluation of the system sensitivity. Observing the same insect species at the same angle but at different distances will allow calibration of the system, which in turn would aid in the quantification of insect sizes.

The heading investigation through modulation spectroscopy yielded both confirmative and non-confirmative results in this study. It has been observed in a laboratory setting that the specular, polarization-maintaining reflexes from insect wings contribute in particular to the higher harmonics of f_0, but also contribute significantly to the lower harmonics. Depending on the relative phase between the specular components and the diffuse wing beats, this contribution can interfere either constructively or destructively. The phase of specular reflexes in the wing-beat cycle depends on the angle of illumination. This angle will shift throughout the day in passive measurements, but is constant in lidar measurements.

Obtaining flight heading information from insects transiting the probe volume would also enable the quantification of insect flight speeds. In the present study, it was demonstrated that a circular probe volume cross section introduces uncertainties in flight speed estimations. This can be overcome by utilizing a quadratic aperture, yielding a quadratic FOV cross section along the entire probe volume. Using a circular detector would yield a circular FOV at the termination, reintroducing the uncertainty at far ranges. Therefore, quadratic sensors and apertures are preferable to circular ones in this application.

There are a number of possible uses for the presented method. It can be implemented horizontally to profile insects in active or passive mode along transects across the landscape. By utilizing an infrared laser with a wavelength where the atmosphere does not scatter sunlight, the method can also be implemented vertically. Another approach to vertical profiling would be to fix the aim of the setup at the Polaris star, which would ensure sunlight impinging on the probe volume at an approximately normal angle at all times. The setup could then be implemented vertically in passive mode. Detection schemes with multiple wavelength- or polarization bands could also be envisioned in both active and passive mode.

Conclusions

We conclude that quadrant sensors can be used to determine the range to organisms or particles transiting the probe volume, and that fluxes can be quantified. We also conclude that the previously suggested model for determining insect flight headings using modulation spectroscopy is insufficient and needs further work. In particular, the effect of specular reflexes on the strength and phase of lower harmonics of f_0 needs to be investigated.

The demonstrated ranging method has the potential to become a widespread tool for monitoring insect abundances and fluxes, particularly in farming environments. Similar to DOAS, which is a widespread method for monitoring gas concentrations in urban environments [33], the demonstrated method is inexpensive and simple to implement. Despite its ease of use and low power requirements, it yields rich information on insect observations. By retrieving range information, insect concentrations and fluxes are resolved in space and time and can be correlated to weather and topography. The method also yields modulation spectra that have a demonstrated capability of species classification. Our method can be adapted and scaled to other geometries where objects, organisms, or particles transit the probe volume. It can also be employed with active illumination, making it a versatile technique that can be used in many different fields of research.

Authors' contributions

MB designed the study, collected the data, and initiated the simulations. SJ finalized the simulations, analyzed the field data, and wrote the manuscript. Both authors took equal part in devising the passive ranging Eq. (1). Both authors read and approved the final manuscript.

Author details

[1] Lund Laser Centre, Department of Physics, Lund University, Sölvegatan 14, 22362 Lund, Sweden. [2] Center for Animal Movement Research, Department of Biology, Lund University, Sölvegatan 35, 22362 Lund, Sweden.

Acknowledgements

We thankfully acknowledge the support and collaboration from Susanne Åkesson which enabled the project, Sandra Török for her participation in the field measurements as well as her previous work and documentation of the dataset, and Alem Gebru, Adam Bäckman, Carsten Kirkeby, Ádám Egri, Annika Söderman and Maren Wellenreuther for their assistance during the measurements.

Competing interests

The authors declare that they have no competing interests.

Availability of data and materials

The datasets used and/or analyzed during the current study are available from the corresponding author on reasonable request.

Consent for publication

Not applicable.

Ethics approval and consent to participate

Not applicable.

Funding

Financial support was given by research grants to Susanne Åkesson from the Swedish Research Council (621-2013-4361) and Lund University. This work was supported by the Swedish Research Council Linnaeus grants (349-2007-8690 & 349-2006-121) and Lund University to the Centre for Animal Movement Research (CAnMove) and to the Lund Laser Centre (LLC). The work is also supported by the Swedish Research Council through a U-forsk grant (348-2014-3481). No funding body had any role in the design of the study, data collection, analysis, interpretation or writing of the manuscript.

Publisher's Note

Received: 19 October 2017 Accepted: 6 April 2018
Published online: 30 May 2018

References

1. Organization WH: World Malaria Report. 2015.
2. Das AJ, Stephenson NL, Davis KP. Why do trees die? Characterizing the drivers of background tree mortality. Ecology. 2016;97:2616–27.
3. Oliveira CM, Auad AM, Mendes SM, Frizzas MR. Crop losses and the economic impact of insect pests on Brazilian agriculture. Crop Prot. 2014;56:50.
4. Vrijheid M, Casas M, Gascon M, Valvi D, Nieuwenhuijsen M. Review: environmental pollutants and child health—a review of recent concerns. Int J Hyg Environ Health. 2016;219:331–42.
5. Sánchez-Bayo F, Goulson D, Pennacchio F, Nazzi F, Goka K, Desneux N. Are bee diseases linked to pesticides? A brief review. Environ Int. 2016;89:7–11.
6. Zhu S, Malmqvist E, Li W, Jansson S, Li Y, Duan Z, Svanberg K, Feng H, Song Z, Zhao G, et al. Insect abundance over Chinese rice fields in relation to environmental parameters, studied with a polarization-sensitive CW near-IR lidar system. Appl Phys B. 2017;123:211.
7. Dao A, Yaro AS, Diallo M, Timbine S, Huestis DL, Kassogue Y, Traore AI, Sanogo ZL, Samake D, Lehmann T. Signatures of aestivation and migration in Sahelian malaria mosquito populations. Nature. 2014;516:387–90.
8. Guan Z, Brydegaard M, Lundin P, Svanberg S, Wellenreuther M, Runemark A, Svensson EI. Insect monitoring with fluorescence lidar techniques: field experiments. Appl Opt. 2010;49:5133–42.
9. Silver JB. Mosquito ecology: field sampling methods. Berlin: Springer; 2008.
10. Majambere S, Massue DJ, Mlacha Y, Govella NJ, Magesa SM, Killeen GF. Advantages and limitations of commercially available electrocuting grids for studying mosquito behaviour. Parasit Vectors. 2013;6:1.
11. Kirkeby C, Wellenreuther M, Brydegaard M. Observations of movement dynamics of flying insects using high resolution lidar. Sci Rep. 2016;6:29083.
12. Eklundh L, Johansson T, Solberg S. Mapping insect defoliation in Scots pine with MODIS time-series data. Remote Sens Environ. 2009;113:1566–73.
13. Müller J, Brandl R. Assessing biodiversity by remote sensing in mountainous terrain: the potential of LiDAR to predict forest beetle assemblages. J Appl Ecol. 2009;46:897–905.
14. Drake VA, Reynolds DR. Radar entomology: observing insect flight and migration. Wallingford: CABI Publishing; 2012.
15. Chapman JW, Drake VA, Reynolds DR. Recent insights from radar studies of insect flight. Annu Rev Entomol. 2011;56:337–56.
16. Melnikov V, Leskinen M, Koistinen J. Doppler velocities at orthogonal polarizations in radar echoes from insects and birds. IEEE Geosci Remote Sens Lett. 2014;11:592–6.
17. Drake VA. Distinguishing target classes in observations from vertically pointing entomological radars. Int J Remote Sens. 2016;37:3811–35.
18. Brydegaard M, Gebru A, Svanberg S. Super resolution laser radar with blinking atmospheric particles—application to interacting flying insects. Prog Electromagn Res. 2014;147:141–51.
19. Repasky KS, Shaw JA, Scheppele R, Melton C, Carsten JL, Spangler LH. Optical detection of honeybees by use of wing-beat modulation of scattered laser light for locating explosives and land mines. Appl Opt. 1839;2006:45.
20. Shaw JA, Seldomridge NL, Dunkle DL, Nugent PW, Spangler LH, Bromenshenk JJ, Henderson CB, Churnside JH, Wilson JJ. Polarization lidar measurements of honey bees in flight for locating land mines. Opt Express. 2005;13:5853–63.
21. Brydegaard M, Gebru A, Kirkeby C, Åkesson S, Smith H. Daily evolution of the insect biomass spectrum in an agricultural landscape accessed with lidar. EPJ Web Conf. 2016;119:22004.

22. Moore A, Miller RH. Automated identification of optically sensed aphid (Homoptera: Aphidae) wingbeat waveforms. Ann Entomol Soc Am. 2002;95:1–8.
23. Potamitis I, Rigakis I. Novel noise-robust optoacoustic sensors to identify insects through wingbeats. IEEE Sens J. 2015;15:4621–31.
24. Chen Y, Why A, Batista G, Mafra-Neto A, Keogh E. Flying insect classification with inexpensive sensors. J Insect Behav. 2014;27:657–77.
25. Runemark A, Wellenreuther M, Jayaweera HHE, Svanberg S, Brydegaard M. Rare events in remote dark-field spectroscopy: an ecological case study of insects. IEEE J Sel Top Quantum Electron. 2012;18:1573–82.
26. Brydegaard M, Merdasa A, Gebru A, Jayaweera H, Svanberg S. Realistic instrumentation platform for active and passive optical remote sensing. Appl. Spectrosc. 2016;70(2):372–85.
27. Gebru A, Rohwer E, Neethling P, Brydegaard M. Investigation of atmospheric insect wing-beat frequencies and iridescence features using a multispectral kHz remote detection system. J Appl Remote Sens. 2014;8:083503.
28. Darzynkiewicz Z, Roederer M, Tanke HJ. Cytometry: new developments. Amsterdam: Elsevier Academic Press; 2004.
29. Jericho SK, Garcia-Sucerquia J, Xu W, Jericho MH, Kreuzer HJ. Submersible digital in-line holographic microscope. Rev Sci Instrum. 2006;77:043706.
30. Brydegaard M. Towards quantitative optical cross sections in entomological laser radar—potential of temporal and spherical parameterizations for identifying atmospheric fauna. PLoS One. 2015;10:e0135231.
31. Malmqvist E, Jansson S, Török S, Brydegaard M. Effective parameterization of laser radar observations of atmospheric fauna. IEEE J Sel Top Quantum Electron. 2016;22:1–8.
32. Török S. Kiloherts electro-optics for remote sensing of insect dispersal. Lund: Lund University; 2013.
33. Platt U, Stutz J. Differential optical absorption spectroscopy: principles and applications. Berlin: Springer; 2008.